HHS Public Access

Author manuscript

Magn Reson Imaging. Author manuscript; available in PMC 2017 February 01.

Published in final edited form as:

Magn Reson Imaging. 2016 February ; 34(2): 209–218. doi:10.1016/j.mri.2015.10.036.

A human brain atlas derived via n-cut parcellation of resting-state and task-based fMRI data

G. Andrew James[1], **Onder Hazaroglu**[2], and **Keith A. Bush**[2]

[1]Psychiatric Research Institute, University of Arkansas for Medical Sciences

[2]Department of Computer Science, University of Arkansas at Little Rock, Little Rock

Abstract

The growth of functional MRI has led to development of human brain atlases derived by parcellating resting-state connectivity patterns into functionally independent regions of interest (ROIs). All functional atlases to date have been derived from resting-state fMRI data. But given that functional connectivity between regions varies with task, we hypothesized that an atlas incorporating both resting-state and task-based fMRI data would produce an atlas with finer characterization of task-relevant regions than an atlas derived from resting-state alone. To test this hypothesis, we derived parcellation atlases from twenty-nine healthy adult participants enrolled in the Cognitive Connectome project, an initiative to improve functional MRI's translation into clinical decision-making by mapping normative variance in brain-behavior relationships. Participants underwent resting-state and task-based fMRI spanning nine cognitive domains: motor, visuospatial, attention, language, memory, affective processing, decision-making, working memory, and executive function. Spatially constrained n-cut parcellation derived brain atlases using (1) all participants' functional data (*Task)* or (2) a single resting-state scan (*Rest*). An atlas was also derived from random parcellation for comparison purposes (*Random*). Two methods were compared: (1) a parcellation applied to the group's mean edge weights (*mean*), and (2) a two-stage approach with parcellation of individual edge weights followed by parcellation of mean binarized edges (*two-stage*). The resulting *Task* and *Rest* atlases had significantly greater similarity with each other (mean Jaccard indices JI= 0.72–0.85) than with the *Random* atlases (JI=0.59–0.63; all $p<0.001$ after Bonferroni correction). *Task* and *Rest* atlas similarity was greatest for the *two-stage* method (JI=0.85), which has been shown as more robust than the *mean* method; these atlases also better reproduced voxelwise seed maps of the left dorsolateral prefrontal cortex during rest and performing the n-back working memory task (r=0.75–0.80) than the *Random* atlases (r=0.64–0.72), further validating their utility. We expected regions governing higher-order cognition (such as frontal and anterior temporal lobes) to show greatest difference between *Task* and *Rest* atlases; contrary to expectations, these areas had greatest similarity between atlases. Our findings indicate that atlases derived from parcellation of task-based and resting-state fMRI data are highly comparable, and existing resting-state atlases are suitable for task-based analyses. We

Corresponding Author: G. Andrew James, PhD, Assistant Professor, Psychiatric Research Institute, University of Arkansas for Medical Sciences, 4301 W. Markham St #554, Little Rock, AR 72205-7199, GAJames@uams.edu.

introduce an anatomically labeled fMRI-derived whole-brain human atlas for future Cognitive Connectome analyses.

1. Introduction

The recent growth of functional neuroimaging research has led to development of human brain atlases that accurately reflect the brain's functional organization. Several such atlases have been generated by applying parcellation approaches to functional magnetic resonance imaging (fMRI) data [1–7]. These approaches identify functionally independent brain regions by first calculating the functional connectivity between all voxels (i.e. the correlation of each voxel's activity timeseries with all other voxels), then using parcellation algorithms (such as the n-cut method, cite) that maximize *within-cluster* voxels' correlations while minimizing *between-cluster* voxels' correlations.

All functional atlases to date – whether encompassing the entire brain [1–4] or specific cortical regions [5–7] – have been derived from resting-state fMRI scans in which participants lie awake in the scanner while not engaged in overt tasks. But functional connectivity patterns change with cognitive task, raising the possibility that atlases derived solely from resting-state data may be suboptimal for studying task-dependent brain activity. As examples, functional connectivity between Broca's and Wernicke's areas dramatically increases during a reading task compared to tongue-movement or rest [8], and connectivity among motor regions increases with finger tapping compared to rest [9]. In both examples, functional connectivity seed maps show clearer boundaries during task than rest, suggesting that a parcellation approach incorporating both resting-state and task-based functional connectivity may produce an atlas with finer characterization of task-relevant regions than an atlas derived solely from resting-state data.

We addressed this potential barrier by deriving two whole-brain atlases from fMRI data acquired through the Cognitive Connectome project [10], an initiative to translate fMRI into patient care by bridging clinical neuropsychology and functional neuroimaging. We derived two atlases: one atlas incorporating data from a single resting-state scan (similar to existing atlases), and a comparison atlas incorporating data from resting-state and task-based scans encompassing motor performance, visual perception, visuospatial judgment, emotional processing, verbal memory, visual memory, working memory, language fluency, attentional conflict, reward processing, and executive function. We hypothesize that a parcellation incorporating both resting-state and task-based fMRI data (a *Task* atlas) will substantially differ from an atlas derived from resting-state data alone (*Rest*). Specifically, we predict that regions recruited during higher-order cognition (such as prefrontal and temporal regions for executive function, language, and memory) will substantially differ in size and shape between atlases, whereas regions involved in less demanding tasks (such as visual and motor regions) will be similar across atlases. We also predict that voxelwise connectivity seed maps of task-based fMRI scans will show stronger spatial correspondence to seed maps derived from the task-based atlas than the resting-state atlas. Finally, we provide the atlas as an anatomically labeled tool for future analyses of the Cognitive Connectome project data.

2. Materials and Methods

2.1. Cognitive Connectome

All Cognitive Connectome study procedures were conducted in the Brain Imaging Research Center at the University of Arkansas for Medical Sciences. Study participation was typically conducted in two sessions on separate days. Session 1 included informed consent, a structured clinical interview (SCID-IV/NP) to determine exclusionary criteria, behavioral surveys and questionnaires (such as the State-Trait Anxiety Inventory and Big Five Personality Inventory), and the first of two hour-long neuroimaging session (with neuroimaging session order counterbalanced across subjects). Session 2 included neuropsychological assessment and the second neuroimaging session. Cognitive Connectome project study procedures are described in full detail elsewhere [10].

2.2. Participants

Thirty-five participants completed both fMRI sessions. (Five additional pilot participants completed both fMRI sessions, but are excluded due to substantial task redesign based upon their feedback.) Table 1 and Supplementary Materials provide descriptions of each fMRI scan, including task design and scan duration. Scans with excessive head motion (i.e. greater than 3mm lateral movement in any direction) were excluded from analyses. Of these 35 participants, 29 were included in the final analysis: 7 with useable data from 12 scans, and 22 with useable data from all 13 scans. The excluded scans included a second resting-state scan (n=2), visual memory (n=2), motor performance (n=1), visual perception (n=1), and executive function (n=1). The twenty-nine participant sample had the following demographics: mean(sd) age = 31(9.9), range 20–50; 10 (34%) male, 19 (66%) female; 19 (66%) self-reporting as White or Caucasian, 12 (41%) as Black or African-American, 1 (3%) as Hispanic or Latino, including 1 participant who self-identified as both Caucasian and African-American; mean(sd) education = 16(2.2) years, range 10–19. All participants were recruited with approval and oversight by the UAMS Institutional Review Board (protocol #130825).

2.3. Image Acquisition and Preprocessing

2.3.1. Image Acquisition—Imaging data were acquired using a Philips 3T Achieva X-series MRI scanner (Philips Healthcare, Eindhoven, The Netherlands). Anatomic images were acquired with a MPRAGE sequence (matrix = 256 × 256, 220 sagittal slices, TR/TE/FA = shortest/shortest/8°, final resolution =0.94 × 0.94 × 1 mm^3 resolution). Functional images for early participants (001–050) were acquired using an 8-channel head coil with an echo planar imaging (EPI) sequence (TR/TE/FA = 2000 ms/30 ms/90°, FOV=240 × 240 mm, matrix = 80 × 80, 37 oblique slices parallel to orbitofrontal cortex to reduce sinus artifact, interleaved ascending slice acquisition, slice thickness = 4 mm, final resolution 3.0 × 3.0 × 4.0 mm^3). For these subjects, one session's resting-state scan was acquired with 3-mm slice thickness to be consistent with data acquired for other BIRC studies. Functional images for later participants (051–079) were acquired using a 32-channel head coil with the following EPI sequence parameters: TR/TE/FA = 2000 ms/30 ms/90°, FOV = 240 × 240 mm, matrix = 80 × 80, 37 oblique slices, ascending sequential slice acquisition, slice thickness = 2.5 mm with 0.5 mm gap, final resolution 3.0 × 3.0 × 3.0 mm^3.

Parameters for the 32-channel coil were selected to reduce orbitofrontal signal loss due to sinus artifact. To assess head coil as a potential confound, we regressed head coil against participants' functional connectivity data (measured as voxelwise seed maps with the dorsolateral prefrontal cortex, see below) to evaluate if choice of head coil significantly influenced functional connectivity (and thus, atlas generation).

2.3.2. Image Preprocessing—All MRI data preprocessing was conducted in AFNI unless otherwise noted [11]. Anatomic data underwent skull stripping, spatial normalization to the icbm452 brain atlas, and segmentation into white matter (WM), gray matter (GM), and cerebrospinal fluid (CSF) with FSL [12]. Functional data underwent despiking; slice correction; deobliquing (to 3×3×3 mm^3 voxels); motion correction (using the 10^{th} timepoint); transformation to the spatially normalized anatomic image; regression of motion parameters, mean timecourse of WM voxels, and mean timecourse of CSF voxels; spatial smoothing with a 6-mm FWHM Gaussian kernel; and scaling to percent signal change. Resting-state scans also underwent bandpass filtering (0.01–0.10 Hz) to remove physiological artifact relating to noise. fMRI scans with head motion exceeding 3mm lateral movement were excluded from subsequent scans. Participants' binarized GM masks were averaged to generate a group-level gray matter mask; voxels with a group mean GM value ≥ 0.5 were included in the parcellation approach described below.

2.4. Analyses

2.4.1. Parcellation—MRI data parcellation utilized the normalized cut (n-cut) approach [1]. This approach used a refinement of graph cutting algorithms that attempt to partition undirected, weighted graphs by assigning the graph's partitions according to a minimized cut cost. The cut cost, cut(A,B), represents the sum of the weights of edges that must be removed from the graph to completely partition the subset of nodes, A, from a disjoint subset of nodes, B. The n-cut algorithm modifies the cut cost by dividing the total sum of edge weights associated with subsets A and B, respectively, thus normalizing the influence between densely and sparsely connected nodes. In application to MRI, graph nodes were represented by individual voxels and graph edges include only those voxels in the 3-dimensional (face and edge adjacent) neighborhood, resulting in 26 edges per voxel. Edge weights were set equal to voxel pair-wise Pearson correlations over the voxels' time-courses. In other words, *n*-cut searched for "fissures" of weak connectivity between neighboring voxels, and set these fissures as boundaries to maximize within-cluster correlations among voxels and minimize correlations of voxels belonging to neighboring clusters.

This n-cut approach also allows two algorithms for group-level parcellation. The *group mean* algorithm averages edge weights across the group prior to the n-cut parcellation. The *group two-stage* algorithm first parcellates each subject's MRI based on their edge weights, then digitizes the first-stage parcellations to produce binary (0 or 1) edge weights which are averages across the group prior to the second n-cut parcellation. Both methods were explored here.

Three region of interest (ROI) group atlases were generated for each method. The first atlas (*Rest*) was constructed entirely from one resting-state scan (comparable to experiments

conducted in [1]). The second atlas (*Task*) was constructed from combined resting-state and task scans, which are concatenated into a single image as follows. Each individual scan was first z-scored voxel-wise; then the scans were concatenated in the time dimension; then the combined scan was z-scored. The third atlas (*Random*) was constructed by setting the edge weights between neighboring voxels to 1 rather than the voxels' Pearson correlation. Thus there are no "fissures" of weak connectivity to guide parcellation, causing voxels to randomly parcellate into equally sized clusters.

All n-cut parcellations were conducted using the experimental source code for the work published in [1] available at https://www.nitrc.org/projects/cluster_roi/. Normalization and concatenation calculations were conducted using Matlab. All experiments were executed on a Hewlett Packard ProLiant DL980 G7 Server (80 processors and 4TB single-addressable memory). Scripts and data are available upon request.

2.4.2. Comparing ROIs across atlases—We compared the similarity (homology) of ROIs across atlas parcellations as follows. Let set I equal all voxels comprising an ROI in Atlas A (ROI_A). The voxels spatially corresponding to the voxels in set I were identified in Atlas B. The values of these voxels indicate the ROI(s) in Atlas B with partial overlap with ROI_A, and the mode of these voxels' values identify the ROI in Atlas B (ROI_B) with the greatest overlap of ROI_A. Letting set J equal all voxel comprising ROI_B, the similarity of ROI_B and ROI_B was calculated using the Jaccard index, or the number of voxels shared by ROI_A and ROI_B divided by the total number of voxels in ROI_A and ROI_B (i.e. intersection $I \cap J$/union $I \cup J$).

2.4.3. Comparing connectivity seed-maps across atlases—We compared the atlases' ability to replicate connectivity seed maps for the left dorsolateral prefrontal cortex (LDLPFC) across two conditions: during wakeful rest and during performance of the n-back working memory task. The LDLPFC was identified from group-level analysis of the n-back task: brain activity was contrasted between 2-back and 0-back conditions for each participant using general linear modeling (GLM) with AFNI's 3dDeconvolve, residual maximum likelihood (REML) analyses accounted for influence of temporal autocorrelation with 3dREMLfit, and mixed-effects meta-analysis identified group-level differences between 2-back and 0-back conditions with 3dMEMA (all scripts available upon request). A 6mm radius spherical ROI was centered upon the LDLPFC (MNI coordinates −44, 23, 31; Figure 3), and voxelwise seed maps were generated by correlating each voxels' activation timeseries with the mean activation timeseries of voxels within the ROI. Atlas seed maps were generated by identifying the atlas seed ROI containing the most voxels from the task-defined ROI, extracting the mean timeseries of voxels comprising each ROI, correlating each ROI timeseries with the atlas seed ROI timeseries, and backprojecting these correlations to GM voxels comprising each atlas. The resulting seed maps (*voxelwise, Task atlas, Rest atlas*) were Fisher z-transformed so that the voxels' correlations approximated linearity, and the three seed maps were compared via pairwise spatial correlation.

3. Results

3.1. Evaluating ROI sizes

ROIs encompassing fewer than 5 voxels (135 mm^3) were removed from each parcellation, as these ROIs were too small to be biologically meaningful. ROIs which were three standard deviations larger than the mean were also removed from each parcellation. This includes a cluster composed of over 2,300 voxels (62,100 mm^3) identified for the *Task, group two-stage* method which covered much of the brain's circumference. Similar implausibly large ROIs have been identified and omitted from other brain atlases [1]. ROI sizes did not significantly differ between atlases, either before removal of artifactual clusters [$F(5,1169)=0.09$, $p<0.99$] or after removal [$F(5,1161)=1.08$, $p<0.37$]. After removal, mean ROI size ranged from 177–186 voxels across parcellations, with standard deviations ranging from 42–50 voxels.

3.2. Evaluating similarity

3.2.1. ROI similarity across all atlases—Table 1 provides mean Jaccard indices (JI) for ROI similarity between atlases. Each combination of dataset and parcellation method yielded an atlas with strong similarity to the random parcellation (mean JI 0.59–0.63). Jaccard indices were skewed toward the highest possible value of 1, prompting use of nonparametric statistics to compare ROI similarity between atlases. ROI JIs were much greater for atlases generated using the same method or same data than for the randomly generated atlases (all Wilcoxon rank sum tests values > 4, all $p < 0.001$ after Bonferonni correction for 8 comparisons). This was particularly true for the *group two-stage* method *Task* and *Rest* atlases; ROI JIs were greater for these atlases ($\mu=0.846$) than for the random parcellation ($\mu=0.645$; z-value>10, $p<0.001$). We replicated these analyses using the Dice coefficient similarity index and found almost perfect correlation ($r=0.99$), supporting our use of the Jaccard index.

3.2.2. Similarity between *All* and *Rest* atlas ROIs—Figure 1 depicts ROIs for the *Task, group two-stage* atlas, and Figure 2 depicts the JI for each ROI compared to its homolog in the *Rest, group two*-stage atlas. 47% of these ROIs had a JI ≥0.90, and 79% had JI ≥0.80. Contrary to hypotheses, greatest similarity was observed for prefrontal cortex, cingulate gyrus, left parietal lobe, and left temporal lobe. Only 5% of ROIs had a JI <0.50. Table 2 lists all ROIs of the *Task, group two-stage* atlas ranked by their similarity to the *Rest, group two-stage* atlas. Regions with lowest similarity (JI<0.50) included right sensorimotor area (middle primary sensory cortex (S1), JI=0.34; inferior S1, JI=0.41; lateral premotor area, JI=0.37;), left sensorimotor area (left S1, JI=0.48; and adjacent left inferior parietal lobule, JI=0.49), regions bordering ventricles (left caudate, JI=0.42; septum pellucidum, JI=0.47; thalamus, JI=0.42), right middle temporal gyrus (medial region, JI=0.33; lateral region, JI=0.33), and right posterior superior parietal lobule (JI=0.40).

3.3. Seed map comparisons

Figure 3 and Table 3 compare left DLPFC seed maps derived via parcellation-atlases or voxelwise approaches. All parcellation-derived seed maps were significantly correlated with voxewise seed maps ($r= 0.64$–0.80, all $p<0.001$). Voxelwise seed maps had stronger

correlation (and thus higher replication) with *Task* and *Rest* atlas seed maps (r= 0.75–0.80) than *Random* atlas seed maps (r= 0.64–0.72). Additionally, *Task* and *Rest* atlas seed maps were highly correlated for resting-state (r=0.89) and n-back task (r=0.92), further emphasizing these atlases' similarity.

Finally, the regression of head coil against DLPFC connectivity seed maps showed no consistent pattern of coil-related differences in connectivity (Table 4). During the n-back task, the 32-channel head coil was associated with greater LDLPFC connectivity among two regions: one located at pre-SMA/dACC and another in right SMA (AlphaSim corrected q<0.05). These regions corresponded with the *Task* atlas's ROIs #200 and #79 – which were highly replicable across *Task* and *Rest* atlases (Table 3, JI=0.93 and 0.85, respectively). Furthermore, no regions showed coil-related significant differences in DLPFC connectivity for the resting-state scans. The lack of replicable, systemic coil-related differences in connectivity across these two tasks suggests that head coil is not influencing functional connectivity patterns, and thus not confounding atlas generation. This finding is consistent with our past findings that head-coil does not significantly influence task-related brain activity [10]

4. Discussion

We report strong similarity between atlases derived via parcellation of resting-state data and atlases derived via parcellation of both resting-state and task-based data. Our findings are consistent with past research suggesting that brain networks are consistently organized across task and rest [13]; we expand upon those findings to suggest that the brain's functionally independent subunits ("nodes") are also consistently represented across task and rest. The similarity between *Task* and *Resting* atlases may partially stem from the necessary incorporation of baseline conditions in fMRI tasks to model task-related changes in brain activity or connectivity. These baseline conditions are low-level cognitive control tasks (such as the 0-back condition of the n-back task) and/or resting-state epochs, which may enforce similar connectivity structure between task-based and resting-state fMRI scans. Nonetheless, the similarity between atlases remains striking given that resting-state epochs compose less than half of the tasks' timepoints.

We also report strong similarity of these atlases to the random parcellations (mean JI=0.59–0.63). Although initially surprising, this may be explained by our decision to constrain the parcellation approach to gray matter voxels, which causes white matter to form consistent boundaries across all parcellations. For example, regions with multiple white matter boundaries (such as the cingulate, which is bounded by white matter to the left, right, and inferior surfaces) have greater constraint in how they may be parcellated, potentially explaining the strong Jaccard Indices between atlases observed in Figure 2.

Leave-one out cross-validation has shown that the *group two-stage* approach generates atlases that are more representative across individuals than the *group mean* approach [1]. We thus limited our comparison of task-based and resting-state parcellations to atlases generated using the *group two-stage* approach. Contrary to hypotheses, task-based and resting-state parcellations had strong similarity (JI≥0.90) for regions involved in higher-order cognition,

including prefrontal cortices, cingulate, and left temporal lobe. We interpret this as evidence that the cognitive processes occurring in the absence of overt task (such as rumination, autobiographical memory retrieval, introspection and theory of mind) are sufficiently similar across rest and diverse tasks to map these regions with high consistency [14;15].

Conversely, we report least similarity for (a) three regions in right sensorimotor cortex, (b) two regions in right superior temporal sulcus, and (c) two regions bordering the left lateral ventricle. The sensorimotor cortex encodes the neural representation of the hand, with significantly greater activity for contralateral hand movement but greater *variability* for ipsilateral hand movement [16], particularly in the context of changing task demand [17]. Given the variety of tasks performed (with 7 tasks requiring right hand responses and 2 requiring both left and right hand responses), greater heterogeneity (less similarity) in right sensorimotor cortex is not surprising given this predominantly (90%) right-hand dominant sample.

The role of the right STG is not as clearly established as the left STG, which is strongly associated with auditory processing [18;19]. Right STG has been implicated in diverse processes such as encoding auditory rhythms [20], multisensory integration [21], and contextual awareness [22]. These processes may be more strongly engaged during task than rest, resulting in variable recruitment of the right STG across tasks and thus dissimilar representation of right STG between task and rest. Perhaps more surprising is the dissimilarity between atlases for striatal regions bordering left lateral ventricle, which show bilateral recruitment for processes such as learning, reward processing, and motor processing [23–28]. Future work will evaluate asymmetric striatal recruitment across tasks to evaluate which cognitions could be leading to the discrepancy in striatal representation between atlases.

Finally, we demonstrate that voxelwise seed maps of left dorsolateral prefrontal cortex (LDLPFC) functional connectivity are more consistently reproduced by the *All* and *Rest* atlas than the *Random* atlas. Interestingly, the *All* and *Rest* parcellations produced a LDLPFC ROI that strongly corresponds to the LDLPFC region identified by the *n*-back task, as indicated by the blue crosshairs in Figure 3. Conversely, the *Random* atlas LDLPFC ROI shows poor correspondence with the task-defined ROI. This finding both reinforces the similarity of the *Task* and *Rest* atlases while demonstrating their superiority over the *Random* atlas in capturing underlying neural organization.

An important caveat is that our parcellations were constrained to brain regions covered across all participants and sessions. Our conservative approach led to incomplete coverage of the inferior orbitofrontal cortex, a region notoriously difficult to image with fMRI due to proximity of air in the sinus cavity which distorts magnetic signal in this region. While combined spin-echo and echo-planar sequences have been developed to optimally image this region [29], these sequences suffer a 50% reduction in temporal resolution, prompting our selection of the standard echo-planar sequence. We contend that our atlas is well-suited for analyzing Cognitive Connectome project data and other fMRI datasets, the majority of which also rely upon echo-planar sequences. However, given the strong similarity between atlases derived from task-based and resting-state data, we conclude that previously published

atlases derived from combined spin-echo/echo-planar sequences are likewise suitable for task-based analyses.

5. Conclusions

We have uploaded a fully labeled atlas to the Neuroinformatics Tool and Resources Center (https://www.nitrc.org/) for public use.[1] Our findings indicate that this atlas is well-suited for analysis of both resting-state and task-based data. Our findings further suggest that existing atlases derived solely from resting-state data are equally suitable for resting-state and task-based analyses.

Acknowledgments

This research was supported by the Translational Research Institute (TRI) at the University of Arkansas for Medical Sciences (UAMS) which is funded by the National Institutes of Health (NIH) Clinical and Translational Science Award (CTSA) program (UL1TR000039); the CTSA KL2 Scholars Program (KL2TR000063; to GAJ). We additionally thank Mr. Jonathan Young and Mrs. Sonet Smitherman for assistance with data collection and maintaining institutional compliance. All authors contributed to the interpretation and writing of this manuscript.

Reference List

1. Craddock RC, James GA, Holtzheimer PE III, Hu XP, Mayberg HS. A whole brain fMRI atlas generated via spatially constrained spectral clustering. Hum Brain Mapp. 2012; 33(8):1914–1928. [PubMed: 21769991]
2. Jones DT, Vemuri P, Murphy MC, Gunter JL, Senjem ML, Machulda MM, et al. Non-stationarity in the “resting brain’s” modular architecture. PLoS One. 2012 Jul 5.:e39731. [PubMed: 22761880]
3. Harrison SJ, Woolrich MW, Robinson EC, Glasser MF, Beckmann CF, Jenkinson M, et al. Large-scale probabilistic functional modes from resting state fMRI. Neuroimage. 2015; 109:217–231. [PubMed: 25598050]
4. Shen X, Tokoglu F, Papademetris X, Constable RT. Groupwise whole-brain parcellation from resting-state fMRI data for network node identification. Neuroimage. 2013; 82:403–415. [PubMed: 23747961]
5. Goulas A, Uylings HB, Stiers P. Unravelling the intrinsic functional organization of the human lateral frontal cortex: a parcellation scheme based on resting state fMRI. J Neurosci. 2012; 32(30): 10238–10252. [PubMed: 22836258]
6. Nelson SM, Cohen AL, Power JD, Wig GS, Miezin FM, Wheeler ME, et al. A parcellation scheme for human left lateral parietal cortex. Neuron. 2010; 67(1):156–170. [PubMed: 20624599]
7. Yeo BT, Krienen FM, Sepulcre J, Sabuncu MR, Lashkari D, Hollinshead M, et al. The organization of the human cerebral cortex estimated by intrinsic functional connectivity. J Neurophysiol. 2011; 106(3):1125–1165. [PubMed: 21653723]
8. He AG, Tan LH, Tang Y, James GA, Wright P, Eckert MA, et al. Modulation of neural connectivity during tongue movement and reading. Hum Brain Mapp. 2003 Feb 25.:222–232. [PubMed: 12599281]
9. Newton AT, Morgan VL, Gore JC. Task demand modulation of steady-state functional connectivity to primary motor cortex. Hum Brain Mapp. 2007; 28(7):663–672. [PubMed: 17080441]
10. Gess JL, Fausett JS, Kearney-Ramos TE, Kilts CD, James GA. Task-dependent Recruitment of Resting State Networks Reflects Normative Variance in Cognition. Brain and Behavior. 2014; 4:650–664. [PubMed: 25328842]
11. Cox RW. AFNI: software for analysis and visualization of functional magnetic resonance neuroimages. Computers and biomedical research, an international journal. 1996; 29:162–173.

[1]Atlas will be uploaded to NITRC upon acceptance of manuscript and/or made available upon the Magnetic Resonance Imaging website, pending further discussion with editors

12. Jenkinson M, Beckmann CF, Behrens TE, Woolrich MW, Smith SM. Fsl Neuroimage. 2011 Oct 08.:782–790. [PubMed: 21979382]
13. Smith SM, Fox PT, Miller KL, Glahn DC, Fox PM, Mackay CE, et al. Correspondence of the brain's functional architecture during activation and rest. Proc Natl Acad Sci U S A. 2009 Jul 22.:13040–13045. [PubMed: 19620724]
14. Buckner RL, Andrews-Hanna JR, Schacter DL. The brain's default network: anatomy, function, and relevance to disease. Ann N Y Acad Sci. 2008 Apr 11.:1–38. [PubMed: 18400922]
15. Andrews-Hanna JR, Saxe R, Yarkoni T. Contributions of episodic retrieval and mentalizing to autobiographical thought: evidence from functional neuroimaging, resting-state connectivity, and fMRI meta-analyses. Neuroimage. 2014; 91:324–335. [PubMed: 24486981]
16. Dassonville P, Zhu XH, Uurbil K, Kim SG, Ashe J. Functional activation in motor cortex reflects the direction and the degree of handedness. Proc Natl Acad Sci U S A. 1997; 94(25):14015–14018. [PubMed: 9391144]
17. Wexler BE, Fulbright RK, Lacadie CM, Skudlarski P, Kelz MB, Constable RT, et al. An fMRI study of the human cortical motor system response to increasing functional demands. Magn Reson Imaging. 1997; 15(4):385–396. [PubMed: 9223039]
18. Peeva MG, Guenther FH, Tourville JA, Nieto-Castanon A, Anton JL, Nazarian B, et al. Distinct representations of phonemes, syllables, and supra-syllabic sequences in the speech production network. Neuroimage. 2010; 50(2):626–638. [PubMed: 20035884]
19. Bitan T, Cheon J, Lu D, Burman DD, Gitelman DR, Mesulam MM, et al. Developmental changes in activation and effective connectivity in phonological processing. Neuroimage. 2007; 38(3):564–575. [PubMed: 17884585]
20. Kung SJ, Chen JL, Zatorre RJ, Penhune VB. Interacting cortical and basal ganglia networks underlying finding and tapping to the musical beat. J Cogn Neurosci. 2013; 25(3):401–420. [PubMed: 23163420]
21. Beauchamp MS. See me, hear me, touch me: multisensory integration in lateral occipital-temporal cortex. Curr Opin Neurobiol. 2005; 15(2):145–153. [PubMed: 15831395]
22. Zucker NL, Green S, Morris JP, Kragel P, Pelphrey KA, Bulik CM, et al. Hemodynamic signals of mixed messages during a social exchange. NeuroReport. 2011; 22(9):413–418. [PubMed: 21602650]
23. Grahn JA, Parkinson JA, Owen AM. The role of the basal ganglia in learning and memory: neuropsychological studies. Behav Brain Res. 2009; 199(1):53–60. [PubMed: 19059285]
24. Knutson B, Cooper JC. Functional magnetic resonance imaging of reward prediction. Curr Opin Neurol. 2005; 18(4):411–417. [PubMed: 16003117]
25. Hikosaka O, Kim HF, Yasuda M, Yamamoto S. Basal ganglia circuits for reward value-guided behavior. Annu Rev Neurosci. 2014; 37:289–306. [PubMed: 25032497]
26. Ena S, de Kerchove dA, Schiffmann SN. Unraveling the differential functions and regulation of striatal neuron sub-populations in motor control, reward, and motivational processes. Front Behav Neurosci. 2011; 5:47. [PubMed: 21847377]
27. Liu X, Hairston J, Schrier M, Fan J. Common and distinct networks underlying reward valence and processing stages: a meta-analysis of functional neuroimaging studies. Neurosci Biobehav Rev. 2011; 35(5):1219–1236. [PubMed: 21185861]
28. Balleine BW, O'Doherty JP. Human and rodent homologies in action control: corticostriatal determinants of goal-directed and habitual action. Neuropsychopharmacology. 2010; 35(1):48–69. [PubMed: 19776734]
29. Heberlein KA, Hu X. Simultaneous acquisition of gradient-echo and asymmetric spin-echo for single-shot z-shim: Z-SAGA. Magn Reson Med. 2004; 51:212–216. [PubMed: 14705064]

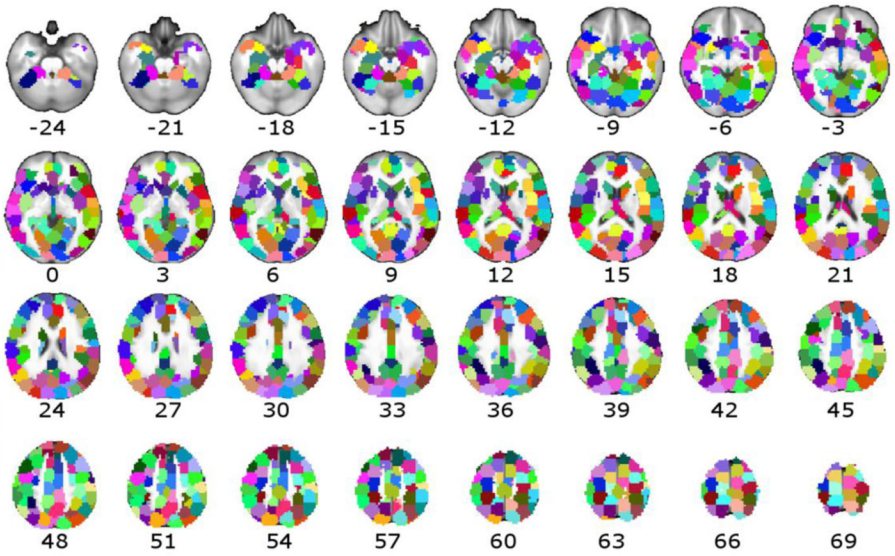

Figure 1. Regions comprising the *Task, group two-stage* atlas

The parcellation derived from 29 healthy participants using the *Group two-stage* method and all task-based and resting-state data is depicted across axial slices (MNI coordinates z=−24 to z=69). Regions of interest (ROIs) are color-coded to maximize contrast between parcellation boundaries. ROIs demonstrate strong bilateral symmetry of ROIs between hemispheres.

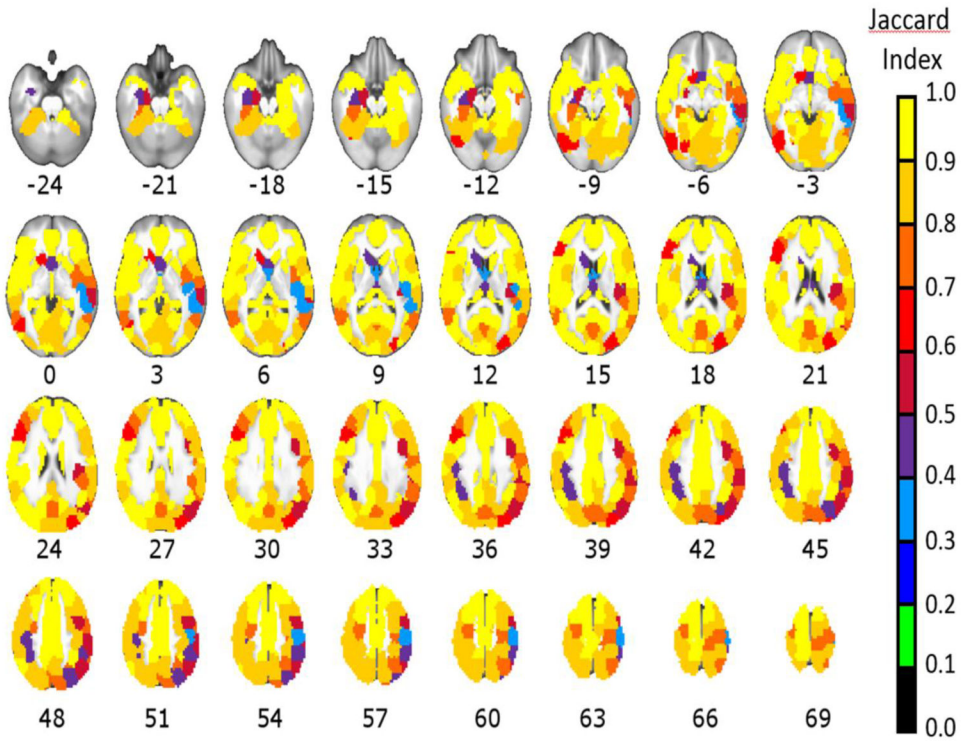

Figure 2. Strong similarity between *Task* and *Rest* atlases

The parcellation derived using the g*roup, two-stage* method and all task-based and resting-state data was compared to the parcellation derived using the *group, two-stage* method but a single resting-state session for each participant. The Jaccard Index (JI) reported overall strong similarity between parcellations (mean JI= 0.85). Contrary to hypotheses, regions associated with higher-order cognition (such as prefrontal and temporal regions) showed strong similarity across task-based and resting-state parcellations. Poorest similarity was observed for ROIs in right sensorimotor area, right superior temporal sulcus, and regions bordering left lateral ventricle.

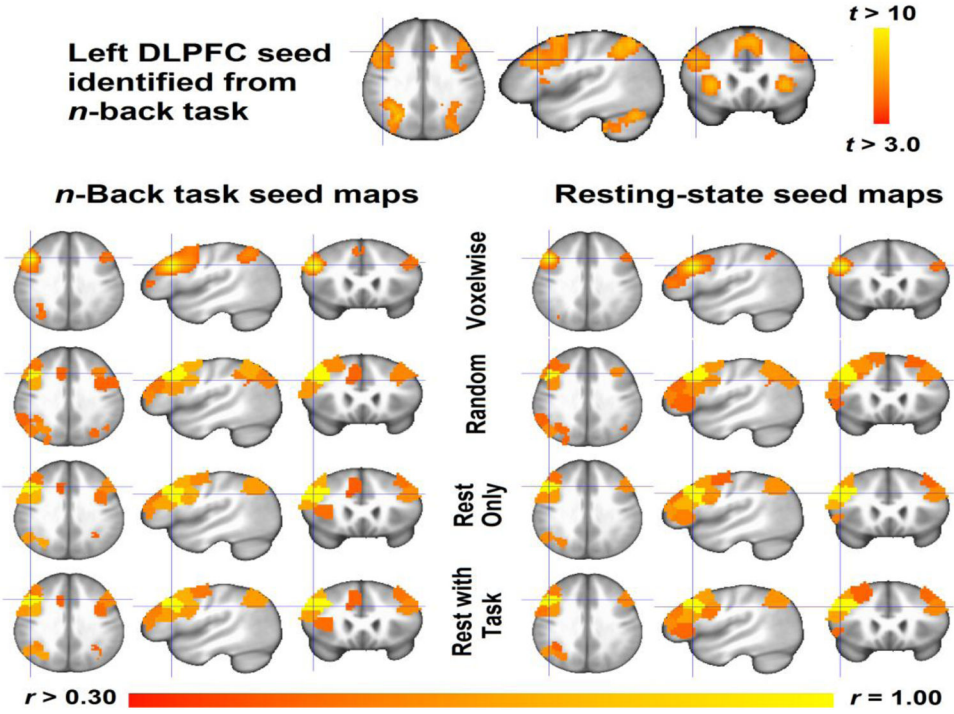

Figure 3. Validation of atlases via task-based and resting-state replications of seed maps

(Top) The *n*-back task elicited greater group-level bilateral dorsolateral prefrontal (DLPFC) and parietal activity for 2-back condition than 0-back condition. Results are displayed a $p<0.005$ uncorrected and contiguous cluster size>2,050mm^3 (76 contiguous voxels) for AlphaSim corrected $q<0.01$. We identified the left DLPFC seed as a 6mm radius ROI centered upon MNI coordinates (−44, 23, 21), indicated by blue crosshairs. (Bottom) Correlation seed maps were generated for the n-back and resting-state data using voxelwise data and mean timecourses of the *Random*, *Resting*, and *Task-based* parcellation atlases. All three atlas seed maps correlated with the voxelwise seed map, although correlations were significantly higher for the *Resting* and *Task* atlases (r=0.75–0.80) than the *Random* atlas (r=0.64–0.72). Note that the left DLPFC ROIs identified from *Resting* and *Task* atlases are centered upon the *n*-back task derived ROI, whereas the *Random* atlas DLPFC ROI is not, probably owing to the incorporation of fMRI data.

Table 1

Descriptions of fMRI tasks

Task	Session†	Duration	Description
Controlled Oral Word Association Task (COWAT)	A	5m 0s	Alternating 15s blocks of Letter or Category word generation separated by 15s rest
Rating affective images (IAPS affect)	A	5m 14s	45 IAPS images (negative, neural, positive) presented in random order for 2.5s with 2–6s inter-stimulus interval
Recognizing affective images (IAPS recognition)	A	10m 12s	90 IAPS images (45 previously seen, 45 new) presented in random order for 2.5s with 2–6s interstimulus interval
Judgment of Line Orientation task (JLOT)	A	4m 16s	15 JLOT trials (self-paced, up to 15s duration) with rest at start of task and each trial completion
N-back	A	8m 0s	Alternating 45s blocks of 0-back or 2-back trials separated by 15s rest
Resting-state	A	7m 30s	Passive viewing of a black fixation cross upon light gray background
Iowa Gambling Task	B	8m 6s – 11m 42s (me an 9m 14s)	Self-paced, participant draws 100 cards of varying reward/loss from 4 decks
Finger tapping	B	3m 0s	18s blocks of index finger tapping (left-right-right-left-right-left) separated by 10s rest
Multi-source Interference Task (MSIT)	B	8m 0s	Alternating 48s blocks of Congruent or Incongruent MSIT trials with 30s rest at start, middle, and end of task
Verbal Paired Associates	B	2m 0s	Ten word pairs presented as consecutive 6s blocks with 30s rest at start and end of task
Resting-state	B	7m 30s	Passive viewing of a black fixation cross upon light gray background
Tower of London	B	3m 26s – 7m 30s (me an 4m 20s)	Self-paced, 24 Tower of London trials (2-, 3- and 4-move) starting with 5s planning phase and ending with 6s rest
Flashing visual checkerboard	B	2m 0s	Four 18s blocks of 4Hz flashing checkerboard separated by 10s rest

†Session order was counterbalanced across participants. Each session began with a resting-state scan, and IAPS affect/IAPS recognition were the second and final scans of session A; otherwise, within-session task order was also counterbalanced across participants.

Table 2

Jaccard Similarity Indices across Atlases

Atlas 1	Atlas 2	Jaccard Index	
		mean	sd
Comparison to Random atlas			
Rest, Random	All, Random	0.645	0.230
Rest, group two-stage	Rest, Random	0.632	0.216
Rest, mean	Rest, Random	0.611	0.228
Task, group two-stage	Task, Random	0.607	0.211
Task, mean	Task, Random	0.588	0.203
Comparison of Atlases by Method			
Task, group two-stage	Rest, group two-stage	0.846	0.144
Task, mean	Rest, mean	0.716	0.221
Comparison of Atlases by Data			
Rest, group two-stage	Resting, mean	0.720	0.200
Task, group two-stage	Task, mean	0.719	0.203

Table 3

Regions of Interest for *Task, Group Two-Stage* atlas ranked by similarity to *Rest, Group Two-stage* Atlas

Region	Jaccard Index	MNI Coordinates			Lobe	Volume (in mm^3)	Label
		X	Y	Z			
38	100	−32.5	35.9	−3	Visual	2106	LaOFG_38
59	100	−0.2	−0.6	34.9	Cingulate	3618	MidCingulate_59
132	100	−17.1	−13.3	25.3	Subcortical	729	Lpo_Caudate_132
35	99	−9.2	−20.4	43.8	Motor	4482	Lpo_pericingulate_35
60	99	−9.5	59.8	24.9	Frontal	4428	LrmPFC/LvmPFC_60
102	99	−47.4	31.7	3.5	Frontal	4509	LIFG_BA45_102
155	99	−0.3	23.4	26.3	Cingulate	4158	dACC_155
73	98	−25.5	56.5	15.6	Frontal	3726	LavlPFC_73
80	98	−25.8	5.8	−13.8	Temporal	4239	LOlfC_80
91	98	18.8	−8.4	−14.8	Temporal	3807	RHPC_CA/Amyg_91
94	98	−11.2	−27.8	10.5	Subcortical	2808	Lthalamus_94
103	98	17.3	−34.3	−18.6	Visual	5373	Rculmen_103
125	98	−34.5	22.4	10.5	Frontal	4617	Lsup_AIns_125
128	98	29.5	−19.6	−13.2	Temporal	3699	RHPC_body_128
197	98	−13.8	3.1	21.2	Subcortical	1809	Lacaudate_197
49	97	45.1	29.3	3.4	Frontal	4293	RIFG_BA45_49
115	97	5.7	33	35.5	Frontal	4752	RAperiCing_95
131	97	−40.1	46.2	12.4	Frontal	4212	LvlPFC_131
143	97	35.1	19.9	−6.8	Frontal	4320	Rinf_AIns_143
186	97	12.2	19.2	8.6	Subcortical	2619	RaCaudate_186
15	96	24.4	8.5	3.6	Subcortical	2646	RAputamen_15
26	96	9.2	−28	10.1	Subcortical	2349	Rthalamus_26
34	96	−1.2	−40.3	−14.6	Cerebellum	2997	Vermis_34
41	96	6.2	42.4	19.8	Cingulate	5130	RrostralACC_MPFC_41
47	96	−7.9	40.5	26.5	Cingulate	5265	LrostralACC_MPFC_47
54	96	−10.5	34.6	53.5	Frontal	3942	LsupFG_54

Magn Reson Imaging. Author manuscript; available in PMC 2017 February 01.

Region	Jaccard Index	MNI Coordinates			Lobe	Volume (in mm^3)	Label
		X	Y	Z			
57	96	6.3	58.5	12.6	Frontal	3321	RvmPFC_57
62	96	−39.1	6.9	35.1	Frontal	4833	LpodlPFC_62
71	96	39.1	46.7	6.3	Frontal	3213	RvlPFC_71
82	96	−10	−39.5	45.9	Parietal	5454	LSPL_5C
85	96	−10	49.4	42	Frontal	3861	LdmPFC_85
113	96	−36.9	20	−5.5	Frontal	5265	Linf_AIns_113
118	96	8.3	7.2	63.7	Cingulate	4509	RpreSMA_118
130	96	34.4	19.6	10.1	Temporal	4509	Rsup_AIns_130
136	96	−7.4	0.2	48.3	Cingulate	4941	LpreSMA/dACC_136
181	96	−25.4	8.3	4.3	Subcortical	3024	LAputamen_181
193	96	29.2	6.4	−15.4	Temporal	3834	ROlfC_193
185	92	46.1	5.2	−14.5	Temporal	4104	RTempPole_185
188	92	−26.5	−36.7	−0.4	Temporal	3294	LHPC_tail_188
190	92	−39.6	−7.9	−0.4	Temporal	5913	Linf_MidIns_190
5	91	−1.1	−51	13	Cingulate	5292	retrosplenial_cortex_5
14	91	−46.8	−55.9	41.3	Parietal	5940	LIPC_PGa_14
19	91	24.4	47.2	34.4	Frontal	5292	RrlPFC_19
40	91	−59.6	−19.7	27.6	Parietal	5751	LIPC_Pfop_40
53	91	−53.8	6.4	27.2	Motor	5400	LdlPFC_53
89	91	8.2	−31.9	43.9	Cingulate	5373	RSPL_5C
158	91	−9.5	−54	35.4	Visual	5265	Lprecu_158
160	91	−26.3	6.1	58	Motor	5778	LFEF_160
27	90	−12.6	−19.7	69.5	Motor	5049	LlatSMA_27
56	90	23.5	−51.2	−10.9	Visual	4887	Rfusiform_56
66	90	42.9	−54.9	18.2	Parietal	5238	RTPOJ_66
70	90	−41.6	−18	14.9	Temporal	4833	LIns_OP1_70
112	90	−54.6	−2.3	−5.2	Temporal	5130	LAinfMTG_112
120	90	−25	23.5	50	Frontal	5454	LsupDLPFC_120

Region	Jaccard Index	MNI Coordinates			Lobe	Volume (in mm^3)	Label
		X	Y	Z			
134	90	−25.3	−86.1	17.8	Visual	5049	Locc_BA18_134
140	90	57.1	−9.2	14.1	Motor	5913	R_OP4_140
149	90	32.6	−36.5	−14.9	Visual	4239	Rfusiform/PHG_149
168	90	−50.8	13.2	8	Frontal	5832	LIFG_BA44_168
11	89	10.5	−43.1	−3.1	Visual	4698	RALingual_11
31	89	−29.2	−53.6	57.1	Parietal	6156	LSPL_7A_31
42	89	22.7	−68.9	−9.1	Visual	5022	Rpofusiform_42
43	89	38.2	−22.5	43.3	Motor	5670	RM1_43
52	89	10.7	−64.2	58.3	Parietal	5022	RSPL_52
167	89	50.4	8.5	2.6	Frontal	5454	RIFG_BA44_167
174	89	41.2	−50.5	−15.8	Visual	5913	Rfusiform/RITG_174
33	88	−39.7	1.1	12.4	Motor	4401	Lsup_MidIns_33
76	88	−30.6	−66.4	41.6	Parietal	6615	LpoIPL_76
87	88	−26.9	−33.6	61.4	Motor	6102	Lmedial_CentralSulcus_87
148	88	3.7	−52.4	48.8	Visual	6129	SPL_7A_148
151	88	−26.5	50.4	29.6	Frontal	4968	LrlPFC_151
163	88	25.3	−36	60.5	Motor	6021	Rmedial_CentralSulcus_163
170	88	0.6	−60.7	−3	Cerebellum	6534	medcbell_170
22	87	−17.5	−33	−17.1	Cerebellum	5076	Lculmen_22
36	87	51	20.1	16.5	Frontal	5076	RIFG_BA44_36
13	86	−12.1	−53.4	61.1	Parietal	5292	LSPL_7A_13
16	86	23.5	13.2	56.5	Frontal	5778	RFEF_16
61	86	52.9	5.3	25.3	Motor	5589	RdlPFC_61
86	86	−56.9	−44.6	25.5	Parietal	6102	LpoSTS_121
95	95	−7.4	21.1	40.6	Cingulate	4968	LAperiCing_95
96	95	−7.1	48.7	6.8	Frontal	4482	LvmPFC/LpgACC_96
105	95	40	40.4	21.4	Frontal	5454	RrlPFC_105
139	95	27.2	37.8	−2.8	Frontal	1404	RaOFG_139

Region	Jaccard Index	MNI Coordinates			Lobe	Volume (in mm^3)	Label
		X	Y	Z			
144	95	9.3	46.4	45	Frontal	4266	RdmPFC_144
156	95	−0.4	−21.7	2.5	N/A	2025	3rdVent_156
162	95	6.2	13.6	44.1	Cingulate	4995	RdorsalperiCing_162
172	95	27.3	53.8	17.7	Frontal	4374	RavlPFC_172
28	94	−0.3	−22.9	32.2	Cingulate	3348	PCC_28
88	94	14.6	−10.4	24.9	N/A	1080	Rpo_Caudate_88
117	94	7.2	45.6	4.2	Frontal	3240	RvmPFC/RpgACC_117
119	94	19.8	−57	4.2	Visual	4401	Rlingual_119
129	94	23	30.1	48.4	Frontal	5724	RsupDLPFC_129
138	94	−12.3	−47.3	−3.1	Visual	5157	Llingual_138
141	94	−18.1	−67.3	23.9	Visual	6561	LlatPrecuneus/V3A_141
166	94	−10.9	16.2	61.7	Frontal	4482	RsupFG_166
177	94	−1.3	−24.7	57.6	Cingulate	5373	midline_SMA_177
178	94	−43.8	8.4	−14.3	Temporal	4482	LTempPole_178
179	94	15.6	−62.2	18.8	Visual	4590	RlatPrecuneus/V3A_179
198	94	−0.5	−2.6	−5.5	N/A	2295	3rdVent_198
199	94	−45.3	−72.2	9.3	Visual	5238	Llatocc_199
18	93	−3.9	−91.1	8.3	Visual	6507	LpoV1_18
21	93	−59.7	−25.6	11.6	Temporal	5724	LSTG_TE3_21
37	93	−1	31.5	0.3	Cingulate	3429	rostralACC_37
64	93	14.7	10.5	−7.5	Subcortical	2970	RNacc_64
67	93	−20.4	−59.8	6.2	Visual	5022	Llingual_67
104	93	9.4	57.6	30.1	Frontal	3780	RrmPFC_104
106	93	−11.4	−2.1	66.8	Cingulate	4590	LpreSMA_106
133	93	−57.6	−5.8	13.3	Motor	5913	L_OP4_133
152	93	−46	−59.2	21	Parietal	5940	LTPOJ_152
175	93	12.2	7.2	18.9	Subcortical	2457	RpoCaudate_175
183	93	7.5	28.1	56.8	Frontal	4779	RsupFG_54

Region	Jaccard Index	MNI Coordinates			Lobe	Volume (in mm^3)	Label
		X	Y	Z			
195	93	32.9	−45.9	41.6	Parietal	5913	RSMG_195
200	93	5.5	−8.7	49.9	Cingulate	5400	RpreSMA/dACC_200
9	92	−56.5	−20.3	−4	Temporal	4617	LmidMTG_9
50	92	−39	−74.9	26.9	Visual	6480	Llat_midOcc_50
58	92	33.1	−83.6	−1.1	Visual	3618	RV3/V4_58
68	92	39.3	−1.6	13.3	Temporal	4212	RsupMidIns_68
75	92	24.6	−36.9	1.5	Temporal	2727	RHPC_tail_75
142	92	−11.4	−38.3	67.8	Motor	4752	LSPL_5L_142
165	92	−43	−32.6	17.9	Motor	5130	LpoIns_165
93	86	−54.6	−35.9	0.6	Motor	4995	LpoMTG_93
107	86	7	−85.8	−2.6	Visual	8829	RpoV1_107
32	85	−43.3	−21.4	57.5	Motor	4779	LlateralCentral_Sulcus_32
78	85	9.9	−74.7	7.6	Visual	5967	RV1_78
79	85	9.5	−11	68.4	Cingulate	4698	RlatSMA_79
81	85	−44.8	−46.3	−14.3	Temporal	3726	LITG_81
83	85	22.6	−67.9	31.9	Visual	6048	RlatPrecuneus_V3A_83
101	85	45.6	23.6	31.4	Frontal	5373	RrostMPFC_101
154	85	58.5	−26.6	13.3	Temporal	4779	RSTG_TE3_154
189	85	58.2	−22.8	30.1	Visual	5697	RIPC_Pfop_189
10	84	39.4	15.8	47.7	Frontal	5616	RsupdlPFC_10
17	84	−32.1	−43.6	−24.4	Cerebellum	5913	LlatCbell_17
29	84	−26.4	37.1	40.2	Frontal	5427	LsupFG_29
63	84	−31.9	−84.2	1	Visual	4320	LV3/V4_63
110	84	−1	−40.7	28.9	Cingulate	3618	dPCC_110
116	84	−15.1	−68.2	52.7	Parietal	5778	LSPL_116
145	84	−41.3	−4.1	51.7	Motor	5076	LLPM_lat_145
146	84	41.9	−74.6	13.6	Visual	5400	Rlatocc_146
44	83	−42.5	−39.4	54.4	Motor	4644	LsupS1_44

Region	Jaccard Index	MNI Coordinates			Lobe	Volume (in mm^3)	Label
		X	Y	Z			
69	83	−8.9	−86.4	26.1	Visual	5211	Lcuneus_69
97	83	9.3	−46.3	65.6	Motor	5643	RSPL_5L_97
123	83	−53.7	−7.4	39.1	Motor	5400	LlatM1_BA4a_123
159	83	43.7	−67.6	−4.2	Visual	5319	Rinf_OccG_159
171	83	33	32.4	36.4	Frontal	5373	RsupFG_171
191	83	6.4	−53.9	32.6	Visual	4941	Rprecu_191
46	82	−27.3	−50.3	−11.1	Visual	5049	Lfusiform_46
84	82	−41.2	13.8	48.3	Frontal	4806	LsupdlPFC_84
126	82	−11.2	−75.7	5.2	Visual	6048	RV1_126
164	82	10.7	−86.5	27.6	Visual	6210	RlatCuneus_164
65	81	−54.3	−32.4	41.1	Parietal	6507	LIPC_PF_65
121	81	58.4	−43.7	21.2	Temporal	5562	RpoSTS_121
150	80	−20.9	−80.8	38	Visual	6075	LmidOccG_150
180	80	24.3	−4.3	58.5	Motor	5994	RLPM_med_180
7	79	−26.9	−12.9	59.7	Motor	6534	LLPM_med_7
20	79	9.8	−29.6	70	Motor	4320	RsupM1_20
90	79	−39.2	38.3	27.8	Frontal	5589	LsupFG_90
77	78	25.8	−19.3	64.1	Motor	5157	RLPM_77
153	78	38.5	−5.7	−1.1	Temporal	5265	Rinf_MidIns_153
74	77	54.8	−7.9	−4.7	Temporal	4212	RAinfMTG_74
127	77	−32.2	−26.7	−13.3	Temporal	4266	LHPC_body/PHG_127
192	77	−0.9	−68.7	20.7	Visual	5697	midV2_192
99	75	13.8	−76.1	45.2	Parietal	4941	RSPL_99
6	74	53.6	−57.4	6.8	Temporal	5211	RpoMTG_6
182	74	−1.5	−72.3	39.5	Visual	5589	midV3/V3A_182
98	73	−54.1	−51.3	8.2	Temporal	5319	LinfTPOJ_98
39	72	25.1	−55.8	57.2	Parietal	6561	RSPL_7P_39
111	72	52.2	−50.5	35.6	Parietal	5265	RIPC_Pga_111

Region	Jaccard Index	MNI Coordinates			Lobe	Volume (in mm^3)	Label
		X	Y	Z			
194	72	42.7	−33.4	20.6	Temporal	4860	RpoIns_194
48	71	51.7	−5.5	38	Motor	5643	RlatM1_BA4a_48
122	69	24.7	−85.9	15.1	Visual	4752	Rocc_BA18_122
184	69	30	−81.5	30.8	Visual	5454	RmidOccG_30
187	68	−45.8	−62.9	−5.1	Visual	5751	Linf_OccG_159
3	67	−49.2	27	21.4	Frontal	4779	LAdlPFC_3
23	66	−42.8	22.9	35.6	Frontal	4860	LrostMPFC_23
196	62	−11.4	15.7	−2.3	Subcortical	2889	LNAcc_196
100	56	41.7	−52	51	Parietal	5103	RIPL_PGa_100
109	56	39.3	−19.4	14	Temporal	4887	RIns_OP1_109
2	55	36.9	6.2	36.1	Frontal	5049	RpodlPFC_2
45	55	57.2	−22.4	−3.6	Temporal	3321	RmidMTG_45
157	55	47.5	−67.3	28.3	Parietal	5913	Rlat_midocc_157
51	54	−25	−10.1	−16.1	Temporal	6048	LHPC_CA/Amyg_51
147	53	53	−34.7	43	Parietal	5454	RIPC_PF_147
169	49	−35.4	−45.2	40.4	Parietal	5238	LSMG_169
124	48	−12.9	16.8	12	N/A	2943	Lpocaudate_124
176	48	−40.7	−21.6	42.8	Motor	5319	LmidS1_176
114	47	0.1	7	5	N/A	3807	SubgenCing_114
135	42	−0.5	−13.1	15.3	Subcortical	2403	thalamus_135
12	41	41	−31.9	56.7	Motor	4428	Rlateral_CentralSulcus_41
30	40	33.2	−68.6	44.7	Visual	6291	RpoIPL_30
24	38	57.8	−39.8	0.7	Temporal	3996	RpoMTG_24
161	37	39.5	−2.7	52.5	Motor	5211	RLPM_lat_161
92	34	47.5	−17.5	50.9	Motor	4347	RlatM1/S1_92
173	33	47.3	−30.4	2.5	Temporal	4644	RpoMTG_173
55	1	−23	−68.7	−9	Visual	4617	Lpofusiform_55
1	0	0	0	0	N/A	0	Garbage_1

Region	Jaccard Index	MNI Coordinates			Lobe	Volume (in mm^3)	Label
		X	Y	Z			
4	0	0	0	0	N/A	0	Garbage_4
8	0	0	0	0	N/A	0	Garbage_8
25	0	0	0	0	N/A	0	Garbage_25
72	0	0	0	0	N/A	0	Garbage_72
108	0	0	0	0	N/A	0	Garbage_108
137	0	0	0	0	N/A	0	Garbage_137

Table 4

Regions of increased voxelwise connectivity to left DLPFC for 32- vs 8-channel head coil (q<0.05)

Cluster	MNI Coordinates			Volume (in mm^3)	Corresponding Region in *Task* Atlas		
	x	y	z		Region	Label	Jaccard index with *Rest* Atlas
1	8	−16	42	8046	200	Right pre-SMA/dorsal cingulate	93
2	5	−16	66	2,133	79	Right SMA	85

Differences reported for n-back task only; no significant coil-related differences observed during resting-state